LETTER

Force loading explains spatial sensing of ligands by cells

Roger Oria[1,2], Tina Wiegand[3,4], Jorge Escribano[5], Alberto Elosegui-Artola[1], Juan Jose Uriarte[2], Cristian Moreno-Pulido[1], Ilia Platzman[3,4], Pietro Delcanale[1], Lorenzo Albertazzi[1], Daniel Navajas[1,2,6], Xavier Trepat[1,2,7,8], José Manuel García-Aznar[5], Elisabetta Ada Cavalcanti-Adam[3,4] & Pere Roca-Cusachs[1,2]

Cells can sense the density and distribution of extracellular matrix (ECM) molecules by means of individual integrin proteins and larger, integrin-containing adhesion complexes within the cell membrane. This spatial sensing drives cellular activity in a variety of normal and pathological contexts[1,2]. Previous studies of cells on rigid glass surfaces have shown that spatial sensing of ECM ligands takes place at the nanometre scale, with integrin clustering and subsequent formation of focal adhesions impaired when single integrin–ligand bonds are separated by more than a few tens of nanometres[3–6]. It has thus been suggested that a crosslinking 'adaptor' protein of this size might connect integrins to the actin cytoskeleton, acting as a molecular ruler that senses ligand spacing directly[3,7–9]. Here, we develop gels whose rigidity and nanometre-scale distribution of ECM ligands can be controlled and altered. We find that increasing the spacing between ligands promotes the growth of focal adhesions on low-rigidity substrates, but leads to adhesion collapse on more-rigid substrates. Furthermore, disordering the ligand distribution drastically increases adhesion growth, but reduces the rigidity threshold for adhesion collapse. The growth and collapse of focal adhesions are mirrored by, respectively, the nuclear or cytosolic localization of the transcriptional regulator protein YAP. We explain these findings not through direct sensing of ligand spacing, but by using an expanded computational molecular-clutch model[10,11], in which individual integrin–ECM bonds—the molecular clutches—respond to force loading by recruiting extra integrins, up to a maximum value. This generates more clutches, redistributing the overall force among them, and reducing the force loading per clutch. At high rigidity and high ligand spacing, maximum recruitment is reached, preventing further force redistribution and leading to adhesion collapse. Measurements of cellular traction forces and actin flow speeds support our model. Our results provide a general framework for how cells sense spatial and physical information at the nanoscale, precisely tuning the range of conditions at which they form adhesions and activate transcriptional regulation.

To explore the spatial sensing of ECM molecules by cells, we investigated a wide array of conditions, considering not only the nanometre-scale distribution of ligands but also substrate rigidity, which is itself a major regulator of focal adhesions[12]. To this end, we developed a two-step protocol to combine polyacrylamide hydrogels with block co-polymer micelle nanolithography[13]. We thereby fabricated hydrogels that have on their surface nanopatterned, quasi-hexagonal arrays of gold nanoparticles (nanodots), functionalized with a small peptide (cyclic arginine–glycine–aspartate, cRGD), which is an integrin ligand (Fig. 1a). Owing to steric hindrance[3,8], this system allows just one integrin protein to bind to each functionalized nanodot; it also allows us to control both nanodot spacing and substrate rigidity.

Because hydrogels swell[14], the spacing of the nanodots was greater on gels than on glass surfaces. This swelling was of approximately 20%, and was not affected by gel rigidity (Extended Data Fig. 1). We seeded human breast myoepithelial cells onto the substrates; the cells attached specifically to the nanodots by using $\alpha 5\beta 1$ integrin proteins to bind the cRGD ligands. Blocking these integrins with an antibody, functionalizing the nanodots with a peptide with low affinity for integrin binding (arginine–glycine–glutamate, RGE)[15], or functionalizing gels with cRGD in the absence of nanodots all inhibited cell attachment (Extended Data Fig. 2).

We then analysed how cells formed adhesion complexes on the substrates as a function of ligand spacing and substrate rigidity. As an initial control, we checked cell behaviour on a stiff substrate (glass). As expected, cells plated on non-patterned glass substrates (which were merely coated with a uniform gold layer and functionalized with cRGD) formed long focal adhesions that were rich in phosphory-lated paxillin protein (Fig. 1b, c). On glass nanopatterned substrates with 30-nm spacing between nanodots, focal adhesions still formed, but were shorter. Cells on substrates with 50-nm or 100-nm spacing between nanodots exhibited only small, dotted adhesions. This confirms the reported maximum distance between bound integrins for focal-adhesion formation[3,5], and indicates a length of between 30 nm and 50 nm for a potential molecular ruler in our system.

Also as expected and previously described[10], cells seeded on very soft polyacrylamide gels formed small adhesive structures resembling nascent adhesions[16] when ligands were spaced 50 nm or 100 nm apart, and formed focal adhesions only above a rigidity threshold (Young's modulus) of 5 kPa (Fig. 1d, e). However, above this threshold we found several striking behaviours. First, focal adhesions formed on gels when ligands were spaced both 50 nm and 100 nm apart, though they did not on glass (Fig. 1b, c). Second, the dependency between focal-adhesion formation and ligand spacing was the reverse of that found on stiff substrates: cells formed longer focal adhesions as ligand spacing increased from 50 nm to 100 nm. Finally, adhesions seemed to collapse (drastically reduce their length) above a second rigidity threshold, which was 30 kPa for 100-nm-spaced substrates, and 150 kPa for 50-nm-spaced substrates. Because focal-adhesion collapse occurred at a lower rigidity for the higher spacing, this led to a regime (150 kPa) in which focal-adhesion length increased with decreasing spacing, reproducing the behaviour found on glass.

Thus, our results show that there is an optimal rigidity for adhesion formation, which decreases as ligand spacing increases. We then confirmed the generality, validity, and implications of these results in different ways. First, we increased ligand spacing on gels to 200 nm. Confirming the trend, this reduced the optimal rigidity even further, to 1.5 kPa (Fig. 1d, e). Second, we checked that different methods of quantifying adhesions led to the same trends. These methods
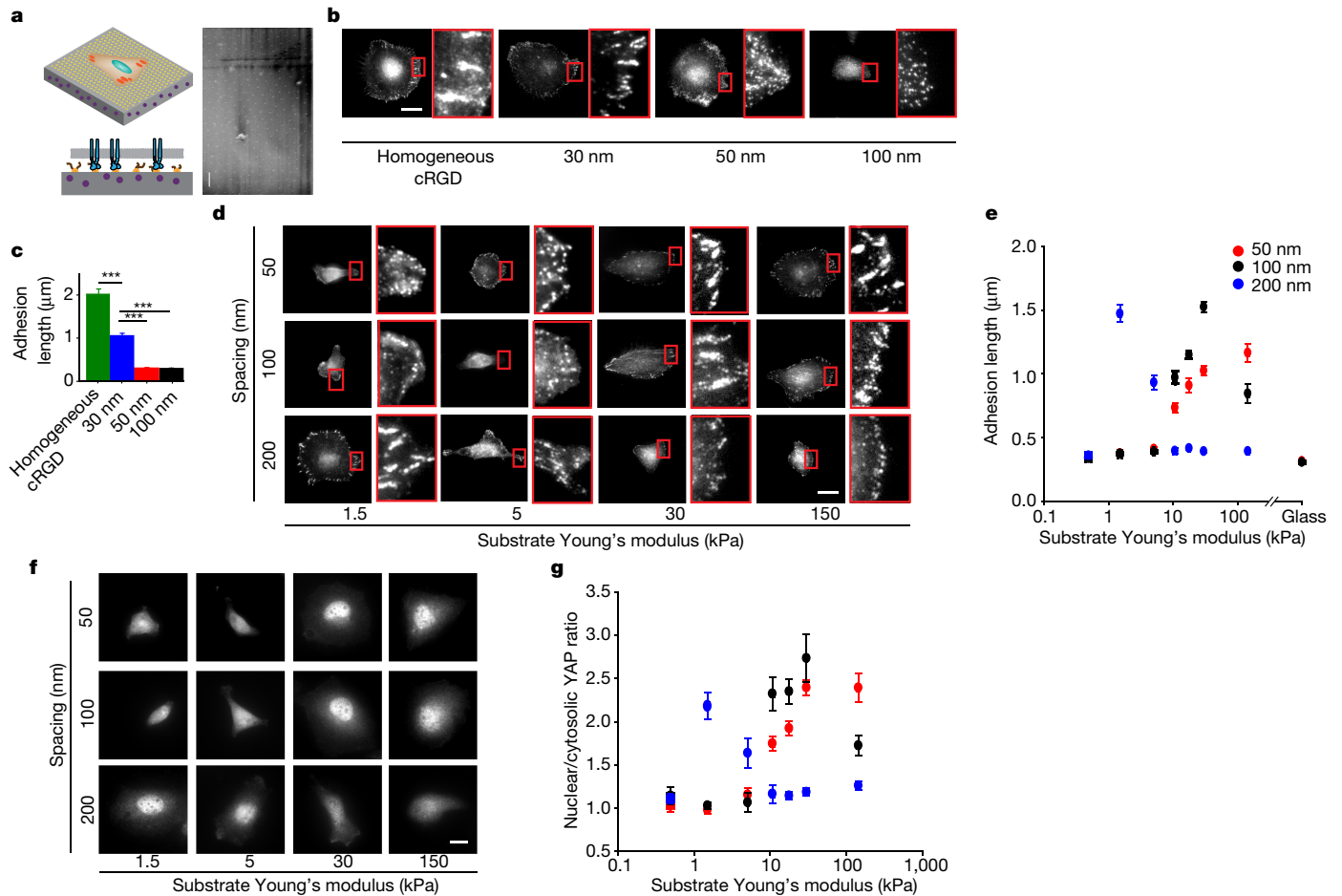
Figure 1 | Increasing ligand spacing promotes the growth of focal-adhesion complexes on intermediate-rigidity substrates, and collapse on high rigidities. a, Top, the nanopatterned polyacrylamide substrates, showing gold nanodots (yellow) on top of polyacrylamide gels with embedded fluorescent beads (purple). A cell adhered through focal adhesions (orange) is shown, with its nucleus in blue. Bottom, spatial configuration of integrin–ECM bonds on the quasi-hexagonal pattern of nanodots coated with cRGD ligands (yellow integrins are in blue). Right, scanning electron micrograph of a 100-nm pattern on a polyacrylamide gel (one of two independent experiments is shown). **b**, Staining for phosphorylated paxillin protein (a component of focal adhesions) in cells seeded on glass substrates coated with either a homogeneous layer of cRGD or quasi-hexagonal distributed cRGD ligands (30-nm, 50-nm and 100-nm spacing). The right-hand image of each pair corresponds to the red rectangle in the left-hand image. **c**, Corresponding quantification of focal adhesion length (mean length of at least three focal adhesions per cell from $n = 12$ cells per condition, from two independent experiments).

*** $P < 0.001$; one-way ANOVA. **d**, Staining of phosphorylated paxillin in cells seeded on polyacrylamide substrates with rigidities (Young's moduli) from 0.5 kPa to 150 kPa, for nanodots spaced 50 nm, 100 nm or 200 nm apart. **e**, Corresponding quantification of focal-adhesion length (mean of at least three focal adhesions per cell from $n = 10/10/11$, 10/12/11, 10/11/11, 10/10/11, 12/11/11, 10/10/11, 11/11/11, 12/12/– cells for 50/100/200-nm-spaced substrates and increasing rigidity; two independent experiments). The effect of both rigidity and spacing was significant ($P < 0.05$; two-way ANOVA). **f**, Staining for the transcriptional regulator YAP in cells seeded on polyacrylamide substrates with rigidities ranging from 0.5 kPa to 150 kPa, with 50-nm-, 100-nm- or 200-nm-spaced nanodots. **g**, Corresponding quantification of nuclear/cytosolic YAP ratio ($n = 15$ cells per condition; two independent experiments); the effect of both rigidity and spacing was significant. ($P < 0.05$, two-way analysis of variance (ANOVA)). Error bars represent mean ± s.e.m. Scale bars represent 200 nm in **a** and 20 μm in **b, d, f**.

involved transfecting green fluorescent protein (GFP)-labelled paxillin into live cells or staining phosphorylated paxillin in fixed cells; and measuring overall paxillin recruitment or measuring focal-adhesion length (Extended Data Fig. 3). Third, we carried out experiments in other cell types (mouse embryonic fibroblasts, human umbilical vein endothelial cells, and MCF 10A breast epithelial cells) and in myoepithelial cells seeded on nanodots coated with a different ligand, the collagen-mimicking GFOGER peptide[16]. The specific thresholds varied, but adhesion formation and collapse, and their dependency on ligand spacing and substrate rigidity, were maintained in all cases (Extended Data Fig. 4). Finally, we analysed the nuclear localization of the mechanosensitive transcriptional regulator YAP[18], which correlates with focal-adhesion formation[10]. Indeed, YAP's nuclear localization closely mirrored focal-adhesion length in all cases, showing a rigidity optimum that depended on ligand spacing (Fig. 1f, g).

Our results—which show adhesion formation on substrates with 50-nm, 100-nm and even 200-nm nanodot spacing, depending on the conditions—are inconsistent with a molecular-ruler mechanism, even if gel deformation were to reduce nanodot spacing. Indeed, although cells could potentially pull on neighbouring ligands to reduce their spacing down to the length of a molecular ruler, this could not explain why, on 1.5 kPa substrates, focal adhesions form only when nanodots are spaced by 200 nm and not shorter distances. To further discard the molecular-ruler hypothesis, we used super-resolution stochastic optical reconstruction microscopy (STORM) of 100-nm-spaced substrates to image paxillin clusters, which correctly reproduced the expected 100-nm spacing (Extended Data Fig. 5). There were no differences in spacing on 30-kPa or 150-kPa substrates, confirming that the increased adhesion formation on the softer 30-kPa substrate was not due to reduced nanodot spacing caused by gel deformability.
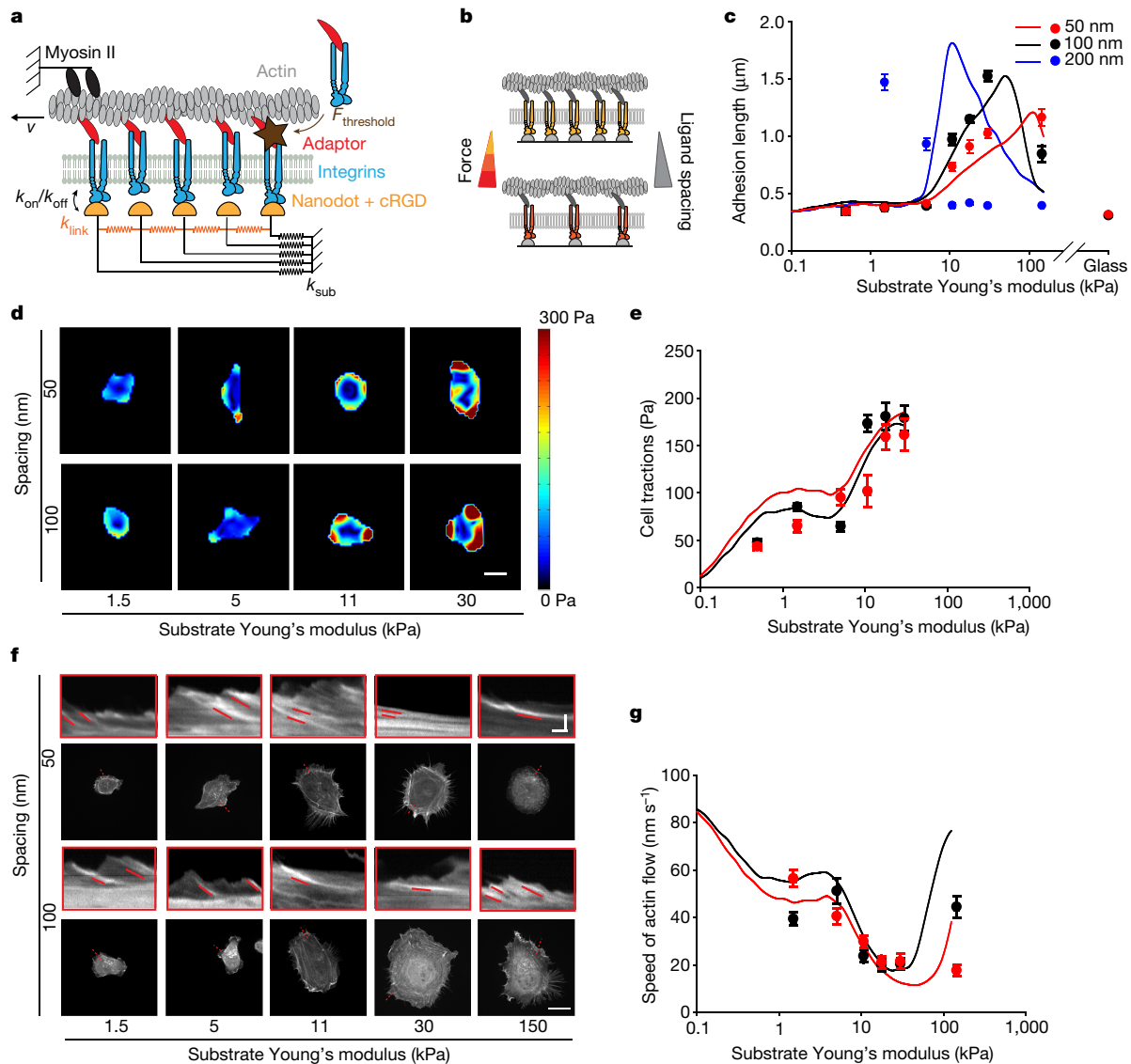
Figure 2 | A molecular-clutch model explains cellular response to ligand spacing. a, The molecular-clutch model. Within cells, myosin motors (black) pull on actin filaments (grey) with velocity v, exerting a force on a set of parallel clutches (formed by adaptor proteins, red, and integrins, blue) which dynamically bind and unbind cRGD ligands (yellow) with on and off rates k_{on} and k_{off}. Mechanosensitivity is introduced by setting a force threshold, $F_{threshold}$, in each clutch that triggers further integrin recruitment when surpassed (brown star). The elastic substrate is represented by springs connecting ligands to the substrate (k_{sub}, black) and to each other (k_{link}, orange). **b**, The effect of ligand spacing on clutch forces: as the spacing decreases, so does the force loading on each individual clutch. **c**, Model predictions (solid lines) and experimental average values (data points, from Fig. 1e) of focal-adhesion length as rigidity increases for differently spaced ligands. Model parameters changed were n_l (180 for 50 nm, 130 for 100 nm and 5 for 200 nm) and the ratio k_{link}/k_{sub} (10 for 50 nm, 5 for 100 nm and

3 for 200 nm). **d**, Examples of cell tractions (colour coding) exerted on substrates of differing rigidity and differing ligand spacing. **e**, Corresponding model predictions (solid lines) and experimental average values of cell tractions ($n = 13/13$, $11/16$, $11/19$, $16/13$, $13/14$ cells for 50/100-nm substrates and increasing rigidity; mean of two independent experiments). **f**, Examples of lifeact-GFP-transfected cells plated on substrates of increasing rigidity. Insets are kymographs showing the movement of actin features along the lines marked in red. The slopes of the traces created by the features (marked with lines) were used to calculate actin speed. **g**, Corresponding model predictions (solid lines) and experimental average values for actin speed (at least three traces were obtained per cell from $n = 7/9$, $9/9$, $11/9$, $8/7$, $8/7$, $9/9$ cells on 50/100-nm-spaced substrates of increasing rigidity; two independent experiments). Scale bars represent 20 μm in the main images and 20 s per 2 μm ($x = y$ axes) in the kymographs. Error bars represent mean ± s.e.m.

Nor could the results be explained by differential regulation of cell spreading, which did not correlate well with adhesion formation, particularly on 50-nm- and 100-nm spaced substrates (Extended Data Fig. 3).

A plausible alternative is regulation by force, as suggested theoretically[19]. Mechanical forces are important in focal-adhesion maturation[20,21], and we have shown[10,11] that focal-adhesion growth in response to rigidity can be explained by force loading in integrins via a molecular-clutch mechanism. Furthermore, force transmission mediated by a molecular clutch is predicted to depend on ligand

density[22,23]. We thus asked whether our results could be explained by a force-regulated, molecular-clutch mechanism.

Our previous molecular-clutch model involves a number of myosin motor proteins pulling on an actin filament, generating a rearward actin flow towards the cell centre. The substrate is modelled by a set of ECM-binding sites (corresponding to the functionalized gold nanodots here) connected to a spring (representing substrate elasticity). Molecular clutches, which comprise integrins and adaptor proteins, dynamically link the actin filament to the ECM substrate. When clutches are engaged, they become progressively loaded as myosin
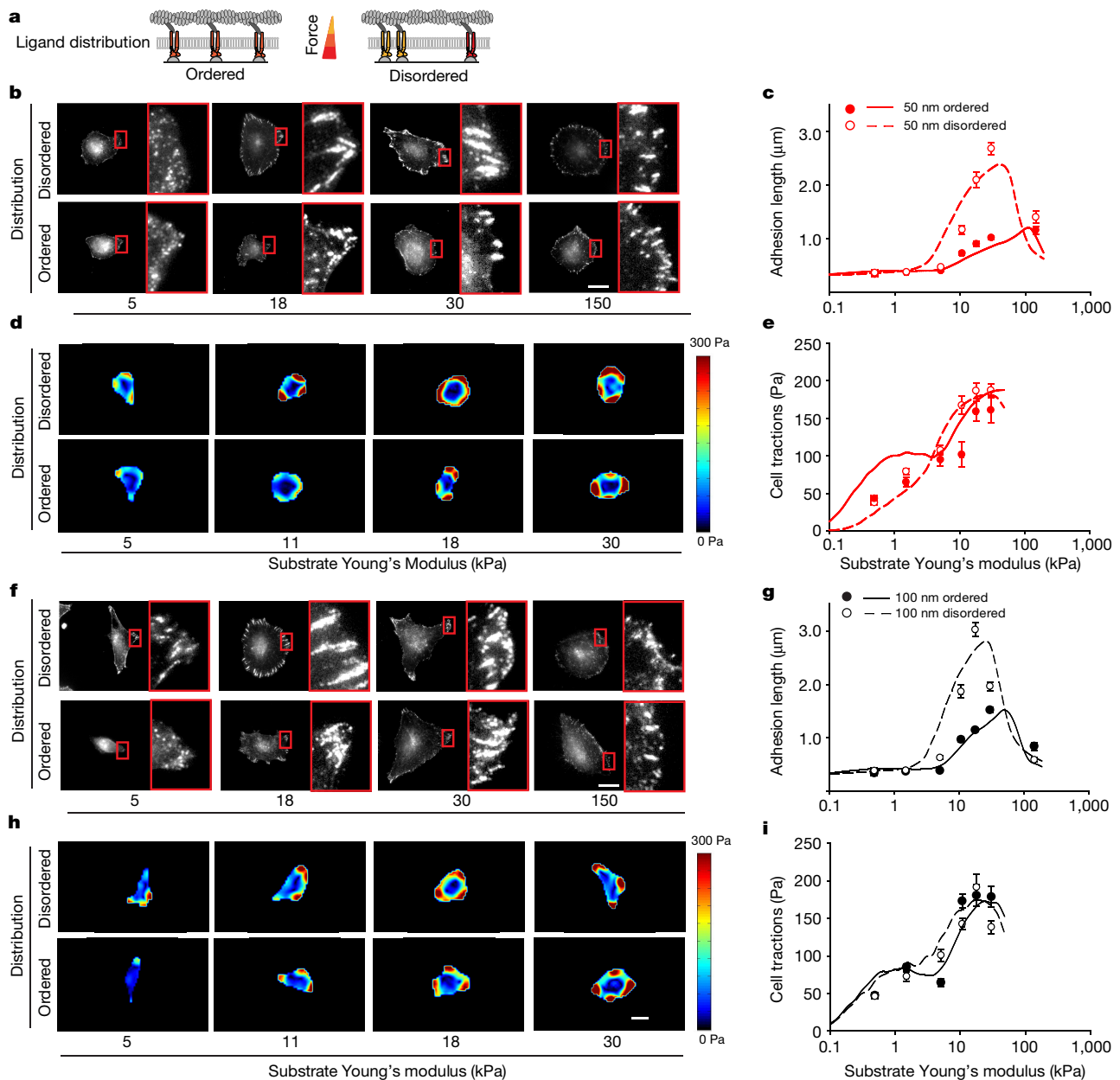
Figure 3 | Ligand disorder promotes adhesion growth, as predicted by the molecular-clutch model. a, Effect of ligand disorder on clutch force. **b**, Staining of phosphorylated paxillin in cells seeded on substrates of varying rigidity, and with ordered or disordered ligand spacing. The left-hand images of each pair are magnifications of the rectangular regions in the right-hand images. **c**, For 50-nm substrates are shown corresponding model predictions (lines) and experimental average values for adhesion length (means of at least three adhesions per cell from $n = 10/10$, $10/10$, $10/10$, $11/10$, $11/12$, $11/10$, $11/11$ cells in disordered/ordered conditions and on substrates of increasing rigidity; two independent experiments). Differences between ordered and disordered conditions were significant ($P < 0.05$; two-way ANOVA). **d**, **e**, For the same 50-nm substrates as in **c** are shown: **d**, examples of cell tractions, and **e**, corresponding model predictions (lines) and experimental average traction values ($n = 14/13$,

12/11, 12/11, 19/16, 16/13, 21/13 cells for disordered/ordered conditions; two independent experiments). Differences between ordered and disordered conditions were significant ($P < 0.05$; two-way ANOVA). **f**, **g**, For 100-nm substrates are shown: **f**, phosphroylated-paxillin staining on ordered and disordered substrates, and **g**, corresponding model predictions (lines) and experimental average traction values (at least three adhesions per cell for $n = 10/10$, $10/12$, $10/11$, $11/10$, $12/11$, $11/10$, $11/11$ cells on disordered/ordered ligands; two independent experiments). **h**, **i**, For the same 100-nm substrates as in **g** are shown: **h**, examples of cell tractions, and **i**, corresponding model predictions (solid lines) and experimental average traction values ($n = 12/13$, $15/16$, $18/19$, $14/13$, $11/16$, $15/14$ cells on disordered/ordered ligands; two independent experiments). Scale bars represent $20\,\mu$m. Error bars represent mean $\pm$ s.e.m.

motors contract the actin filament. Mechanosensitive growth of focal adhesions is modelled by defining a force threshold in each clutch—a force which we previously identified as that leading to unfolding of the actin–integrin adaptor protein talin[10]. If any individual clutch surpasses this threshold before disengaging, it triggers a mechanosensing event that grows adhesions by increasing integrin recruitment. As integrins are recruited, the fraction of integrin-bound ligands increases, allowing adhesions to better withstand force.

To consider the effects of ligand distribution, we expanded this model in two ways (Fig. 2a; see Methods and Extended Data Table 1 for model description and parameters). First, we modelled ligand spacing by using springs to connect ligands not only to the substrate (with a spring constant k_{sub}), but also to each other (with a spring constant k_{link}). In this way, and as expected for an elastic substrate, forces applied to one ligand also deform its neighbours. Increasing k_{link} increases this effect on neighbours, modelling the increased mechanical
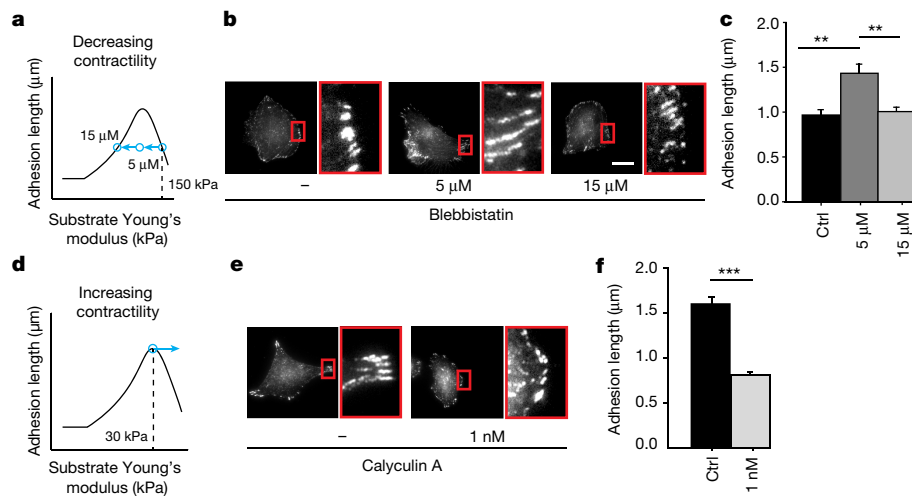
Figure 4 | Myosin contractility regulates adhesion growth according to model predictions. a, Using the myosin inhibitor blebbistatin at concentrations of $5\,\mu M$ or $15\,\mu M$ progressively decreases contractility in cells with collapsed adhesions (150 kPa substrate, 100-nm ligand spacing); this should first bring adhesion length to its maximum, and then decrease it again. **b**, Staining for phosphorylated paxillin in control (−) and blebbistatin-treated cells on 150 kPa substrates with 100-nm ligand spacing. **c**, Corresponding quantification of adhesion length (mean of at least three adhesions per cell from $n = 14$ cells per condition; two independent experiments). **d**, Using calyculin A to increase contractility in cells with maximum adhesions (30 kPa substrate; 100-nm spacing) should decrease adhesion length. **e**, Staining for phosphorylated paxillin in control and calyculin-A-treated cells on 30 kPa substrates with 100-nm spacing. **f**, Corresponding quantification of adhesion length (mean of at least three adhesions per cell from $n = 15$ cells per condition; two independent experiments; two-tailed Student's t-test). Scale bars represent $20\,\mu m$. **, $P < 0.01$; ***, $P < 0.001$. Error bars, mean ± s.e.m.

coupling between ligands that would result from reduced spacing. Second, we imposed a maximum integrin recruitment, because integrin clustering cannot grow indefinitely, but will be restricted by integrin packing and by the physical size of focal adhesions, stress fibres, and cells themselves.

We then used this model to evaluate the role of ligand spacing. As the number of clutches is reduced and their spacing increases, the force exerted by myosin is distributed among fewer clutches, increasing the force loading on each individual clutch (Fig. 2b). This has no effect on very soft substrates, where force loading remains too low to reach the force threshold in any case, and adhesions do not grow. However, as rigidity increases, clutches with higher spacing are more likely to reach the force threshold, increasing integrin recruitment. Because these focal adhesions grow more, they also reach their maximum recruitment at a lower rigidity. At this point, the increased force loading caused by increased rigidity can no longer be compensated by further integrin recruitment, and the adhesion collapses. Thus, this framework can explain the experimental differences. Accordingly, running the computational model with a base set of parameters (Extended Data Table 1) and modifying only the number of ECM ligands (n_l) and their coupling (k_{link}) correctly reproduces the effect of ligand spacing on focal adhesions (Fig. 2c). For 200-nm substrates, we note that the experimental effects were even larger than the range that the model could predict.

To test this model further, we examined its predictions regarding substrate–cell force transmission and actin flows. Our molecular-clutch model[11] predicts an initial increase in force transmission with rigidity, then a plateau or even a slight decrease, and finally an increase until adhesions and forces collapse. As ligand spacing decreases, the plateau is shifted to lower rigidities, and lower forces. We verify these predictions here by measuring them experimentally using traction force microscopy at all rigidities except 150 kPa (for which cell-induced gel displacements were too small to resolve). Although agreement with experiments was not exact in all cases, running the model with the same parameters used above correctly reproduced the trends and relative differences of measured experimental tractions (Fig. 2d, e). Regarding actin flows, the clutch model predicts that they should be anti-correlated with forces[24], because increased force transmission impairs and slows myosin function. Indeed, measured actin flows did show opposite trends to forces in response to both rigidity and ligand

spacing, and were correctly reproduced by the model using the same parameters (Fig. 2f, g). Interestingly, actin flow measurements were available for 150 kPa substrates, allowing us to visualize the regime inducing adhesion collapse (for 100-nm spacing). As predicted by the model, this collapse resulted in increased actin flows (Fig. 2f, g).

We then explored whether force loading regulated by a molecular clutch could explain cell responses to not only overall ligand density, but also ligand distribution. We used substrates with the same density of nanodots and the same mean interparticle distance, but with a disordered rather than ordered quasi-hexagonal distribution (Extended Data Fig. 6)[8]. Because of this spatial disorder, the model predicts that force will be distributed less evenly among clutches (Fig. 3a). This would lead some clutches to experience high loads, increasing the likelihood of surpassing the mechanosensing force threshold, favouring focal-adhesion growth, and shifting focal adhesion collapse to lower rigidities. We verified this prediction experimentally using substrates with 50-nm spacing (Fig. 3b, c) and 100-nm spacing (Fig. 3f, g): in both cases, focal-adhesion growth at intermediate rigidities was increased drastically, and focal-adhesion collapse moved to lower rigidities. Of note, and unlike with ordered patterns, disordering the pattern allowed us to visualize focal adhesion collapse on 50-nm polyacrylamide substrates. The effect of pattern disorder was successfully modelled by modifying only the parameter that represents ligand spacing (k_{link}), to which we assigned not a constant value for all ligands, but a distribution of random values centred on a mean (Fig. 3c, g). In terms of force transmission, the model predicts that, owing to the increased adhesion formation, disorder eliminates the plateau observed at intermediate rigidities, leading to a monotonic force increase with rigidity up to focal-adhesion collapse. This was verified experimentally, and was modelled successfully with the same parameters (Fig. 3d, e, h, i). Notably, disordering the pattern on 100-nm substrates shifted the onset of focal adhesion collapse to a rigidity low enough (30 kPa) to measure force transmission. This allowed us to verify the prediction that focal-adhesion collapse at high rigidities is also associated with a decrease in force transmission (Fig. 3i).

Finally, we verified a fundamental hypothesis of the model: that focal-adhesion collapse at high rigidities is due to excessive loading of integrin–ECM bonds, which can no longer be compensated with adhesion growth. This hypothesis leads to the counterintuitive

prediction that in this 'collapsed' regime, decreasing force loading (for instance by impairing myosin function) should lead to adhesion growth. To confirm this, we seeded cells on rigid 150 kPa gels with 100-nm-spaced nanodots, thereby generating collapsed focal adhesions. One hour after seeding, we treated cells with the myosin inhibitor blebbistatin. As predicted, using a low concentration of blebbistatin (5 μM) resulted in focal-adhesion growth (Fig. 4a–c) compared with the control condition—effectively putting cells in the intermediate force-loading regime where focal-adhesion growth is favoured (Fig. 4a). Also as expected, using a higher concentration of blebbistatin (15 μM) reversed the effect, as force loading was disrupted enough to bring cells to the low-rigidity regime where focal adhesions are also impaired (Fig. 4a–c). Conversely, increasing myosin contractility using calyculin A[25] in cells with the largest adhesions (100-nm spacing, 30 kPa) brought cells to the collapsed regime, decreasing adhesion length (Fig. 4d–f).

The field of cell–matrix adhesion is mature, and several studies have addressed how adhesions are regulated by molecular interactions[26–28] and physical signals[10,20,29,30]; there is wide consensus that cells respond to increases in both rigidity and ligand density by promoting adhesion growth[3,4,10,11,31]. Strikingly, we find here the opposite behaviour in response to both factors. This behaviour is explained not by a distance-sensing mechanism *per se*, but by regulation of molecular force loading, within a predictive model that integrates the effects of rigidity, ligand distribution, and contractility. The resulting cellular response includes the surprising feature of adhesion collapse under high load, which can explain previous findings on stiff substrates showing how ligand molecular length regulates adhesion stability[32], and how increasing ligand spacing renders adhesions unstable[7,19] and unable to sustain large forces on integrins over time[33]. Our results provide a general framework of how cells sense spatial and physical information at the nanoscale, precisely tuning the range of conditions at which they form adhesions and activate transcriptional regulation via YAP. This mechanism might be harnessed by cells in the myriad of physiological and pathological processes that are regulated by mechanical factors and ECM characteristics.

1. Lu, P., Weaver, V. M. & Werb, Z. The extracellular matrix: a dynamic niche in cancer progression. *J. Cell Biol.* **196**, 395–406 (2012).
2. Daley, W. P., Peters, S. B. & Larsen, M. Extracellular matrix dynamics in development and regenerative medicine. *J. Cell Sci.* **121**, 255–264 (2008).
3. Arnold, M. *et al.* Activation of integrin function by nanopatterned adhesive interfaces. *ChemPhysChem* **5**, 383–388 (2004).
4. Cavalcanti-Adam, E. A. *et al.* Lateral spacing of integrin ligands influences cell spreading and focal adhesion assembly. *Eur. J. Cell Biol.* **85**, 219–224 (2006).
5. Altrock, E., Muth, C. A., Klein, G., Spatz, J. P. & Lee-Thedieck, C. The significance of integrin ligand nanopatterning on lipid raft clustering in hematopoietic stem cells. *Biomaterials* **33**, 3107–3118 (2012).
6. Amschler, K., Erpenbeck, L., Kruss, S. & Schön, M. P. Nanoscale integrin ligand patterns determine melanoma cell behavior. *ACS Nano* **8**, 9113–9125 (2014).
7. Cavalcanti-Adam, E. A. *et al.* Cell spreading and focal adhesion dynamics are regulated by spacing of integrin ligands. *Biophys. J.* **92**, 2964–2974 (2007).
8. Huang, J. *et al.* Impact of order and disorder in RGD nanopatterns on cell adhesion. *Nano Lett.* **9**, 1111–1116 (2009).
9. Schvartzman, M. *et al.* Nanolithographic control of the spatial organization of cellular adhesion receptors at the single-molecule level. *Nano Lett.* **11**, 1306–1312 (2011).
10. Elosegui-Artola, A. *et al.* Mechanical regulation of a molecular clutch defines force transmission and transduction in response to matrix rigidity. *Nat. Cell Biol.* **18**, 540–548 (2016).
11. Elosegui-Artola, A. *et al.* Rigidity sensing and adaptation through regulation of integrin types. *Nat. Mater.* **13**, 631–637 (2014).
12. Plotnikov, S. V., Pasapera, A. M., Sabass, B. & Waterman, C. M. Force fluctuations within focal adhesions mediate ECM-rigidity sensing to guide directed cell migration. *Cell* **151**, 1513–1527 (2012).
13. Lohmüller, T. *et al.* Nanopatterning by block copolymer micelle nanolithography and bioinspired applications. *Biointerphases* **6**, MR1–MR12 (2011).
14. Ahmed, E. M. Hydrogel: preparation, characterization, and applications: a review. *J. Adv. Res.* **6**, 105–121 (2015).
15. Hersel, U., Dahmen, C. & Kessler, H. RGD modified polymers: biomaterials for stimulated cell adhesion and beyond. *Biomaterials* **24**, 4385–4415 (2003).
16. Lawson, C. *et al.* FAK promotes recruitment of talin to nascent adhesions to control cell motility. *J. Cell Biol.* **196**, 223–232 (2012); erratum **196**, 387 (2012).
17. Emsley, J., Knight, C. G., Farndale, R. W., Barnes, M. J. & Liddington, R. C. Structural basis of collagen recognition by integrin alpha2beta1. *Cell* **101**, 47–56 (2000).
18. Dupont, S. *et al.* Role of YAP/TAZ in mechanotransduction. *Nature* **474**, 179–183 (2011).
19. de Beer, A. G. *et al.* Force-induced destabilization of focal adhesions at defined integrin spacings on nanostructured surfaces. *Phys. Rev. E* **81**, 051914 (2010).
20. Riveline, D. *et al.* Focal contacts as mechanosensors: externally applied local mechanical force induces growth of focal contacts by an mDia1-dependent and ROCK-independent mechanism. *J. Cell Biol.* **153**, 1175–1186 (2001).
21. Wolfenson, H., Bershadsky, A., Henis, Y. I. & Geiger, B. Actomyosin-generated tension controls the molecular kinetics of focal adhesions. *J. Cell Sci.* **124**, 1425–1432 (2011).
22. Bangasser, B. L. & Odde, D. J. Master equation-based analysis of a motor-clutch model for cell traction force. *Cell. Mol. Bioeng.* **6**, 449–459 (2013).
23. Bangasser, B. L., Rosenfeld, S. S. & Odde, D. J. Determinants of maximal force transmission in a motor-clutch model of cell traction in a compliant microenvironment. *Biophys. J.* **105**, 581–592 (2013).
24. Chan, C. E. & Odde, D. J. Traction dynamics of filopodia on compliant substrates. *Science* **322**, 1687–1691 (2008).
25. Peterson, L. J. *et al.* Simultaneous stretching and contraction of stress fibers in vivo. *Mol. Biol. Cell* **15**, 3497–3508 (2004).
26. Humphries, J. D. *et al.* Vinculin controls focal adhesion formation by direct interactions with talin and actin. *J. Cell Biol.* **179**, 1043–1057 (2007).
27. Kanchanawong, P. *et al.* Nanoscale architecture of integrin-based cell adhesions. *Nature* **468**, 580–584 (2010).
28. Choi, C. K. *et al.* Actin and alpha-actinin orchestrate the assembly and maturation of nascent adhesions in a myosin II motor-independent manner. *Nat. Cell Biol.* **10**, 1039–1050 (2008).
29. Prager-Khoutorsky, M. *et al.* Fibroblast polarization is a matrix-rigidity-dependent process controlled by focal adhesion mechanosensing. *Nat. Cell Biol.* **13**, 1457–1465 (2011).
30. Oakes, P. W., Beckham, Y., Stricker, J. & Gardel, M. L. Tension is required but not sufficient for focal adhesion maturation without a stress fiber template. *J. Cell Biol.* **196**, 363–374 (2012).
31. Engler, A. *et al.* Substrate compliance versus ligand density in cell on gel responses. *Biophys. J.* **86**, 617–628 (2004).
32. Pallarola, D. *et al.* Interface immobilization chemistry of cRGD-based peptides regulates integrin mediated cell adhesion. *Adv. Funct. Mater.* **24**, 943–956 (2014).
33. Liu, Y. *et al.* Nanoparticle tension probes patterned at the nanoscale: impact of integrin clustering on force transmission. *Nano Lett.* **14**, 5539–5546 (2014).

METHODS

Preparation of nanopatterned substrates on glass surfaces. Nanopatterned substrates were prepared as described[3,4,7]. Briefly, polystyrene(x)-b-poly(2-vinylpyridine)(y) diblock copolymers (PolymerSource Inc.) and polystyrene standard (Alfa Aesar) were dissolved in toluene and stirred for 24 hours at room temperature. Different compositions were used to generate ordered and disordered substrates with different spacing (Extended Data Table 2). HAuCL$_4$·3H$_2$0 (Sigma-Aldrich) was added to the micellar solutions with a specific loading parameter defined as $L = n[HAuCL4]/n[P2VP]$. For disordered structures the micellar gold solution was mixed with a polystyrene solution in a 1/1 ratio. 10 μl of the solution were spin-coated (WS-400A-6NPP/Lite, Laurell Technologies Cooperation) onto round coverglasses of 12 mm diameter, previously cleaned with piranha solution. Samples were treated with oxygen plasma (TePla 100-E, 0.4 mbar, 150 W, 10 min) to remove the polymer matrix.

Transfer of nanopatterns to polyacrylamide gels. Nanostructured glass surfaces were activated with ultraviolet light for 30 min, incubated in 10 mM N,N'-bis-(acryloyl)cystamine (Sigma-Aldrich) in ethanol in the dark for 1 hour, and washed thoroughly with pure ethanol. Next, nanostructured surfaces were dried with nitrogen. Polyacrylamide gels were prepared as described[11]. Briefly, glass-bottom dishes were incubated with a solution of acetic acid, 3-(trimethoxysilyl)propyl methacrylate (Sigma) and ethanol (1/1/14), and washed three times with 96% ethanol. A solution containing 0.5% ammonium persulphate, 0.2% tetramethylethylenediamine (Sigma), and 2% fluorescent 200-nm red carboxylated nanobeads (Invitrogen) was mixed with different concentrations of acrylamide and bis-acrylamide to make gels of different rigidities (see Extended Data Table 3). 10 μl of this solution were then placed in the centre of glass-bottom dishes and covered with 12-mm nanostructured surfaces. After 20 min of gel polymerization, hydrogels were soaked in phosphate-buffered saline (PBS) and incubated in the oven for 72 hours at 37 °C, allowing them to swell. Hydrogels were then stabilized at room temperature and the patterned glass surfaces were removed carefully from the hydrogel. Hydrogels with nanopatterned nanodots were gently washed with PBS and then incubated with 25 μM cRGD-thiol (cyclo [Arg–Gly–Asp]–D-Phe–Lys(2-aminohexanoic acid–mercaptopropionic acid), PCS-31062-PI, Peptides International) at room temperature for 4 hours. Afterwards, cRGD-conjugated nanopatterned hydrogels were washed five times (for at least 10 min each time) to remove unbound peptides before cell seeding. For GFOGER experiments, after removing the glass surfaces, gels were incubated with 1 mM of the hetero-bifunctional linker 11-mercaptoundecanoyl N-hydroxysuccinimide ester (MU-NHS) (Prochimia) for 3 hours, then with 1 μM of GFOGER peptide overnight. GFOGER-conjugated nanopatterned hydrogels were washed five times (for at least 10 min each time) to remove unbound peptides before cell seeding.

Substrate characterization by scanning electron microscopy (SEM). Nanostuctured surfaces were sputtered with carbon (low-vacuum coater EM ACE200, Leica) and imaged by SEM (Leo1530, Zeiss) with an in-lens detector and 5 kV acceleration voltage at working distances between 9 mm and 11 mm. Polyacrylamide hydrogels with embedded gold nanodots were vitrified, mounted in a liquid-nitrogen-cooled stage, and transferred to a freeze-fracture system (EM BAF060, Leica). Samples were heated to −90 °C, kept in vacuum for 45 min to sublimate the water at the interfaces, and coated with carbon. Samples were further transferred to the cryo-SEM (Ultra 55 FE-SEM, Zeiss) by an evacuated liquid-nitrogen-cooled shuttle (BAL-TECH VLC 100). Images were recorded at low-temperature conditions ($T = -130 \pm 5$ °C) and low acceleration voltages of 1–1.5 kV because of the low conductivity of the samples, with a working distance of 3 mm. Resulting electron micrographs were analysed in ImageJ (National Institutes of Health) by measuring the distances between a gold nanoparticle and its k-nearest neighbours ($k = 6$ for ordered nanostructures; $4 < k < 8$ for disordered nanostructures) for at least 300 particles of two or more individual nanostructures per condition.

Cell culture and reagents. Human breast myoepithelial immortalized cell lines have been described previously[11,34]. We cultured them in Hams-F12 (Sigma, N4888) media supplemented with 10% foetal bovine serum (FBS), 1% penicillin streptomycin, hydrocortisone (1 μg ml^{-1}), epidermal growth factor (EGF; 10 ng ml^{-1}) and insulin (5 μg ml^{-1}). Human umbilical vein endothelial cells (HUVECs) were purchased from Lonza (CC-2517) and cultured in endothelial growth medium-2 (EGM-2; Lonza CC-4176). Mouse embryonic fibroblasts (MEFs) have been described[35], and were cultured in Dulbecco's modified eagle medium (DMEM; LifeTechnologies, 41965-039) media supplemented with 10% FBS and 1% penicillin streptomycin. Mammary epithelial cells (MCF 10A) were purchased from ATCC and cultured in DMEM-F12 (LifeTechnologies, 21331-020) with 5% horse serum, 1% penicillin streptomycin, EGF (20 ng ml^{-1}), hydrocortisone (0.5 μg ml^{-1}), cholera toxin (100 ng ml^{-1}), and insulin (10 μg ml^{-1}). Myoepithelial cells were authenticated in their laboratory of origin through

expression of the proteins integrin β4, P-cadherin, cytokeratin 17, and desmoglein 3. Other cell lines (used only to verify the generality of our findings) were not authenticated. For all experiments, cells were gently washed with PBS twice, trypsinized, and resuspended in media without FBS. After centrifugation, cells were seeded on hydrogels in media without FBS. To block α5β1 integrins, cells were incubated with an anti-α5β1 antibody (30 μg ml^{-1}, clone JBS5–MAB1969, Millipore) for 30 min before seeding. Cell attachment was evaluated 1 hour after seeding. For blebbistatin experiments, cells were treated with the indicated concentrations of blebbistatin (CalBiochem) for 30 min. For calyculin A experiments, cells were treated with the indicated concentration (Merck Millipore) for 30 min. All cells tested negative for mycoplasma contamination.

Traction force measurements. Traction force measurements were carried out as described[10,11]. Briefly, cells seeded on gels were placed on an inverted microscope (Nikon Eclipse Ti). Single cells were tracked for 3 hours while we acquired phase-contrast images of the cells and fluorescence images of the embedded nanobeads using a ×40 objective. Cells were then trypsinized, and an image of bead position in the relaxed state of the gel was acquired. By comparing bead positions with and without cells, a map of gel deformations caused by cells was first obtained using custom particle-imaging-velocimetry software. Then, after assuming that gel displacements were caused by forces exerted by cells in the cell–gel contact area, we calculated the corresponding map of cell forces using a previously described Fourier transform algorithm[36]. The average forces per unit area exerted by each cell were then calculated. Force measurements for each cell were taken once per hour during the measurement, and the average value for all time measurements was used.

Rearward-flow measurements. To measure the rearward flow of actin filaments, we transfected cells with LifeAct-GFP using a jetPRIME transfection kit (Polyplus transfection) one day before measurements. Cells were then plated on gels of varying rigidity, and imaged every second for 2 min with ×60 oil-immersion objective (numerical aperture (NA) 1.40) with spinning-disc confocal microscopy (Andor). For each cell, kymographs were obtained at the cell periphery, and actin speed was measured from the slope of actin features observed in the kymographs. In cells plated on 0.5 kPa gels, actin features were so diffuse that no reliable slopes could be measured in kymographs.

Immunostaining and adhesion quantification. For fluorescence staining of cell–substrate adhesions, cells were fixed with 4% paraformaldehyde, permeabilized with 0.1% Triton X-100, and labelled first with primary antibody against either phosphorylated paxillin (Cell Signaling 2541S, 1/50 dilution) or YAP (clone 63.7 produced in mice; Santa Cruz catalogue no. sc-101199, 1/200 dilution) for 1 hour at room temperature, and then with anti-rabbit or anti-mouse Alexa-conjugated secondary antibody (Invitrogen) for 1 hour at room temperature. Fluorescence images were then acquired with a ×60 oil-immersion objective (NA 1.40) using a Nikon Eclipse Ti microscope. To quantify adhesion lengths, we identified focal adhesions manually and measured their length. To provide an alternative quantification unbiased by the identification of specific structures, we also quantified the average intensity of phosphorylated-paxillin staining in regions at the cell edge containing both adhesions and surrounding areas, as described[11]. Then, we subtracted the background intensity value calculated from neighbouring cell areas lacking adhesions. The measured trends as a function of both rigidity and ligand density were the same in both quantifications. The degree of nuclear localization of YAP was assessed by calculating the ratio of YAP fluorescence in the nuclear region to YAP fluorescence in the immediately adjacent cytoplasmic region. Nuclear and cytoplasmic regions were previously determined by co-staining the nucleus with Hoechst 33342.

Measurements of gel rigidity. The rigidity (Young's modulus) of polyacrylamide gels was measured by atomic force microscopy as described[37]. Briefly, measurements were made with a custom-built atomic force microscope attached to an inverted optical microscope (Nikon TE200). Silicon nitride pyramidal tips with an effective half-angle θ of 20° and a nominal spring constant of $k = 0.01$–0.03 N m^{-1} were used (MLCT, Bruker). The actual spring constant was calibrated by thermal tuning using the simple harmonic oscillator model[38]. The Young's modulus was measured by recording ten force-displacement curves with a peak-to-peak amplitude of 6 μm and a frequency of 1 Hz. Three points near the gel centre were selected in each gel, separated 5 μm from each other. For each rigidity, six or more gels produced in two batches were measured. To compute the Young's modulus (E), we fitted the Hertz model equation for pyramidal tips to the force-displacement curves. The equation was fitted for an effective indentation of 1,000 nm for all rigidities except 150 kPa, where 500 nm was used.

STORM imaging and distance assessment. To perform direct STORM (dSTORM) imaging, we mounted immunostained cells on gels of different rigidity on a 24 mm × 24 mm glass coverslip using Vectashield mounting medium (H-1000). For image acquisitions, the samples were flipped and placed on the

microscope's sample holder. This allowed the excitation light to pass through the optically matched layer of Vectashield and to be focused on the focal adhesions located at the interface between the cells and the gel substrate. F8811 spheres (Life Technology) on the gel surface allowed for the correction of mechanical drift during acquisition, while the mounting medium allowed for the photoswitching of the fluorophores necessary to perform dSTORM. dSTORM images were acquired using a Nikon N-STORM 4.0 system configured for total internal reflection fluorescence (TIRF) imaging. Alexa647-labelled secondary antibodies were imaged by means of a 647-nm laser (160 mW) while F8811 spheres were imaged using a 488-nm laser (80 mW). No activation ultraviolet light was used. Fluorescence was collected using a Nikon ×100, 1.49 NA oil-immersion objective and passed through a quad-band pass dichroic filter (97335 Nikon). Images were acquired onto a 128×128 pixel region (pixel size 0.16 μm) of a Hamamatsu ORCA–Flash 4.0 camera with an integration time of 5 ms. A total of 50,000 frames was acquired for the 647 channel. Every one hundred imaging frames, one image of the 488 channel was acquired to perform drift correction. STORM images were analysed with the STORM module of the NIS element Nikon software, which generates a list of localizations by Gaussian fitting of blinking dyes in the acquired movie of conventional microscopic images. To avoid overcounting, the software counts blinkings detected in consecutive frames as single. For pattern analysis of focal adhesions, the lists of localizations corresponding to focal-adhesion regions (size about 2.5 μm) were imported and converted in binary images with a pixel size of 3 nm, using a custom Matlab script. Then, binary images were dilated, and clusters identified. A threshold radius was set to discard single blinks not belonging to the cluster. A first analysis of the patterns was then performed with a previously developed Matlab script[39,40] to calculate the pair-correlation functions of cluster patterns up to distances of 900 nm from the identified clusters. Additionally, the centroid of each cluster was identified and the distance of the nearest neighbour was calculated with custom Matlab script.

Statistical analysis. Data reported throughout the manuscript are mean ± s.e.m. Statistical analyses were done with two-tailed Student's t-test when two cases were compared, and with analysis of variance (ANOVA) tests when more cases were analysed. If data did not meet normality criteria, equivalent non-parametric tests were used. No statistical methods were used to predetermine sample size.

Implementation of the molecular-clutch model. *Base model.* The present implementation of the molecular-clutch model is based on a model that has been described in detail[11], which was in turn based on previous implementations[22–24]. Briefly, the model considers a given number of myosin molecules, n_m, pulling on an actin fibre, which in the absence of load contracts at a rearward speed v_u. The substrate is represented by a set of ligands n_l (here, cRGD-functionalized gold nanodots) connected to springs representing substrate elasticity. The actin fibre binds to ligands dynamically through molecular clutches, which represent a complex containing an adaptor protein and integrin. Those clutches have characteristic on and off rates k_{ont} and k_{off}. The off rate (in units of s^{-1}) depends on force as a catch bond, which we modelled according to reported experimental values for the strength of fibronectin–α5β1 bonds[41]. k_{ont} (in units of μm^2 s^{-1}) is the true on-rate for each ligand, which must be multiplied by the available density of integrins (d_{int}) to provide an effective on rate k_{on} with units of s^{-1}. The model is implemented as a Monte Carlo stochastic simulation that starts with all clutches disengaged and actin flowing freely. As the simulation progresses and clutches engage, they pull on the substrate, loading force on the clutches and affecting k_{off}. In addition, force exerted by the substrate on actin slows the myosin motors linearly, which are assumed to stall and stop completely at a force of $n_m \times F_m$, where F_m is the stall force of an individual motor. To model mechanosensitive adhesion growth (reinforcement), if individual clutches exceed a given force threshold, $F_{threshold}$, before disengaging, integrins are recruited. This is implemented by increasing d_{int} by a factor d_{add}. In previous work, we identified this mechanosensitive event as the unfolding of talin[10]. The simulation is run for 100 s with time steps of 2 ms, and run 20 times per condition to obtain average results.

Model expansion. To the model described previously and summarized above, we added two main features to model the effect of substrate spacing and distribution. First, we simply introduced a maximum value for d_{int} ($d_{int,max}$) to model the fact that integrin recruitment has a physical limit. To calculate a parameter that is predictive of adhesion size, in simulations we multiplied d_{int} by the fraction of bound clutches. To compare this with experimental adhesion lengths, we scaled model predictions for cells on 100-nm substrates as a function of rigidity to fall between the maximum and minimum experimental values. All other conditions were scaled by using the same 100-nm reference to retain the relative differences predicted by the model. The second and most important new feature was an improvement of the elastic characterization of the system. In our previous models, the substrate was modelled simply as a set of ligands connected to each other with a rigid rod, which was in turn connected to an elastic spring. Whereas this effectively modelled

substrate rigidity, deformation in all ligands was always the same; it did not allow us to model the elastic coupling between ligands—that is, the fact that a force applied to a ligand will deform neighbouring ligands to a lesser extent as the distance increases. To introduce this, we modelled the substrate not as a single spring, but as a network of springs, where each ligand had a spring connecting it to the substrate (k_{sub}) and one connecting it to neighbouring ligands (k_{link}) (Fig. 2a). For each ligand, its force, F_i, and displacement from rest position, x_i, were then calculated as:

$$F_i = k_{sub}x_i - k_{link}(x_i - x_{i-1}) + k_{link}(x_{i+1} - x_i)$$

At each time step, bound ligands were displaced by the amount of actin movement during the step (providing a known x_i), and unbound ligands were considered to be under zero load (providing a known F_i). This led to a system with n_l linear equations and n_l unknowns, corresponding to the forces of bound ligands and the positions of unbound ligands. After resolving the system, the total force exerted by all ligands was calculated. The degree of mechanical coupling between ligands (modelled by k_{link}) will depend on how forces are transmitted between nanobeads both through the cell cytoplasm and through the polyacrylamide gels. Those nanoscale parameters are essentially inaccessible experimentally and thus k_{link} values were merely adjusted to fit the data. Importantly, however, this approach correctly reproduced the fact that local forces will induce decreasing deformations as distance increases. To take into account the fact that the overall rigidity of the system depends on both k_{sub} and k_{link}, we used these values to calculate an effective network constant, k_{net}, corresponding to the spring constant obtained when pulling on one ligand connected to the entire network. We calculated k_{net} as an iterative process as:

$$k_i = k_{sub} + ((k_{link})^{-1} + (k_{sub})^{-1})^{-1} \text{ for } i = 2$$

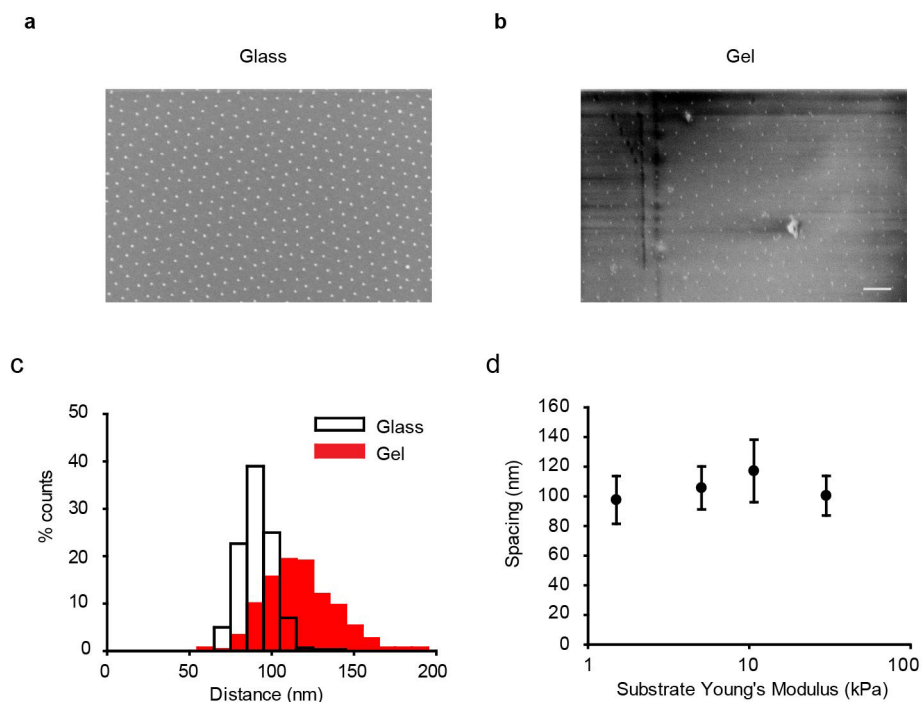$$k_i = k_{sub} + ((k_{link})^{-1} + (k_{i-1})^{-1})^{-1} \text{ for } 3 \leq i \leq n_l/2 - 1$$

$$k_{net} = k_{sub} + 2((k_{link})^{-1} + (k_{n_l/2 - 1})^{-1})^{-1} \text{ for } i = n_l/2$$

The factor 2 in the last expression corresponds to considering the ligands both to the right and to the left of the one being pulled. Although this calculation corresponds to the ligand at the centre of the system, we note that, with the parameters used, k_{net} quickly converged and was largely independent of either n_l or ligand position within the system. This k_{net} was then used to calculate an equivalent substrate Young's modulus by assuming a characteristic adhesion radius, r_0, as described[11,42]. The same characteristic radius was used to convert the one-dimensional model output of force into tractions (force per unit area).

Model parameters and prediction. All model parameters and their origins are described in Extended Data Table 1. The same base set of parameters was used to model all conditions, and the different conditions were modelled by modifying only the relevant parameters in the relevant direction. Specifically, the effect of increased ligand spacing was modelled by decreasing the number of clutches, n_l, and the coupling between ligands, k_{link}. More precisely, both k_{sub} and k_{link} scaled with rigidity, and to model ligand spacing we altered their ratio (k_{link}/k_{sub}). The effect of disorder was modelled by introducing a different value of k_{link} to each clutch, rather than a constant value. Following the long-tailed distribution of distances observed in Extended Data Fig. 4, we chose the values of k_{link} to be randomly distributed according to a Poisson distribution, with a peak corresponding to the value used in the ordered simulations. Of note, using a Gaussian rather than a Poisson distribution led to the same relative trends. Regarding model predictions, those concerning adhesion formation and the effect of ligand distribution are discussed in the main text. However, an interesting point to add is that of the two parameters modified in the simulations (n_l and k_{link}/k_{sub}), n_l is the one responsible for shifting the optimal rigidity for adhesion formation, confirming previous analyses[22,23]. By contrast, k_{link}/k_{sub} serves to modulate the height of the peak. Predictions regarding rigidity and force/actin flow have been discussed extensively[10,11,24]. Briefly, in the absence of adhesion reinforcement and recruitment, the molecular-clutch model predicts a biphasic force–rigidity relationship, in which forces first increase and then decrease with rigidity. The introduction of force-dependent reinforcement triggers adhesion growth and force increase above a rigidity threshold, reverting the downward force trend predicted at high rigidities. Depending on the specific threshold, reinforcement can eliminate the high-rigidity downward trend completely if the threshold is low (leading to a monotonically increasing force–rigidity curve), or only partially. In this case, the force–rigidity curve first increases, then plateaus or even decreases slightly, and then increases again because of reinforcement. We see both cases here: in ordered configurations (Fig. 2), we see the plateau; in disordered configurations (Fig. 3), the threshold is shifted to lower rigidities and we see a monotonic curve.
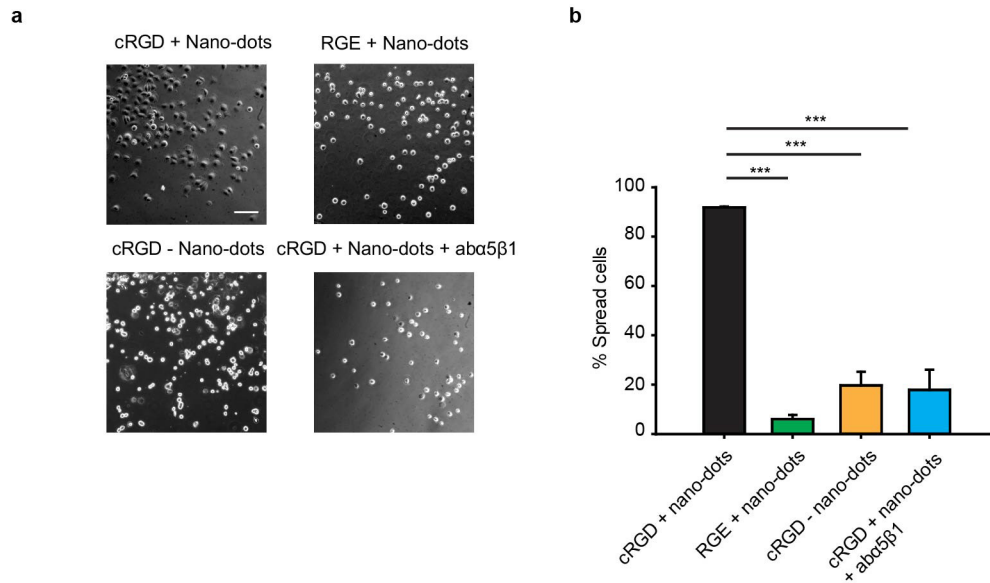
Data availability and code availability. The data that support the findings of this study, and the Matlab code used to generate the computational model, are available from the corresponding author on reasonable request.

34. Allen, M. D. *et al.* Altered microenvironment promotes progression of preinvasive breast cancer: myoepithelial expression of $\alpha v \beta 6$ integrin in DCIS identifies high-risk patients and predicts recurrence. *Clin. Cancer Res.* **20,** 344–357 (2014).
35. Roca-Cusachs, P. *et al.* Integrin-dependent force transmission to the extracellular matrix by alpha-actinin triggers adhesion maturation. *Proc. Natl Acad. Sci. USA* **110,** E1361–E1370 (2013).
36. Butler, J. P., Tolic-Norrelykke, I. M., Fabry, B. & Fredberg, J. J. Traction fields, moments, and strain energy that cells exert on their surroundings. *Am. J. Physiol. Cell Physiol.* **282,** C595–C605 (2002).
37. Alcaraz, J. *et al.* Microrheology of human lung epithelial cells measured by atomic force microscopy. *Biophys. J.* **84,** 2071–2079 (2003).
38. Hutter, J. L. & Bechhoefer, J. Calibration of atomic-force microscope tips. *Rev. Scient. Instr.* **64,** 1868–1873 (1993).
39. Sengupta, P., Jovanovic-Talisman, T. & Lippincott-Schwartz, J. Quantifying spatial organization in point-localization superresolution images using pair correlation analysis. *Nat. Protocols* **8,** 345–354 (2013).
40. Veatch, S. L. *et al.* Correlation functions quantify super-resolution images and estimate apparent clustering due to over-counting. *PLoS One* **7,** e31457 (2012).
41. Kong, F., García, A. J., Mould, A. P., Humphries, M. J. & Zhu, C. Demonstration of catch bonds between an integrin and its ligand. *J. Cell Biol.* **185,** 1275–1284 (2009).
42. Ghibaudo, M. *et al.* Traction forces and rigidity sensing regulate cell functions. *Soft Matter* **4,** 1836–1843 (2008).
43. Molloy, J. E., Burns, J. E., Kendrick-Jones, J., Tregear, R. T. & White, D. C. Movement and force produced by a single myosin head. *Nature* **378,** 209–212 (1995).
44. Litvinov, R. I. *et al.* Resolving two-dimensional kinetics of the integrin alphaIIbbeta3-fibrinogen interactions using binding-unbinding correlation spectroscopy. *J. Biol. Chem.* **287,** 35275–35285 (2012).
45. Roca-Cusachs, P., Iskratsch, T. & Sheetz, M. P. Finding the weakest link— exploring integrin-mediated mechanical molecular pathways. *J. Cell Sci.* **125,** 3025–3038 (2012).

a

Glass

b

Gel

c

d

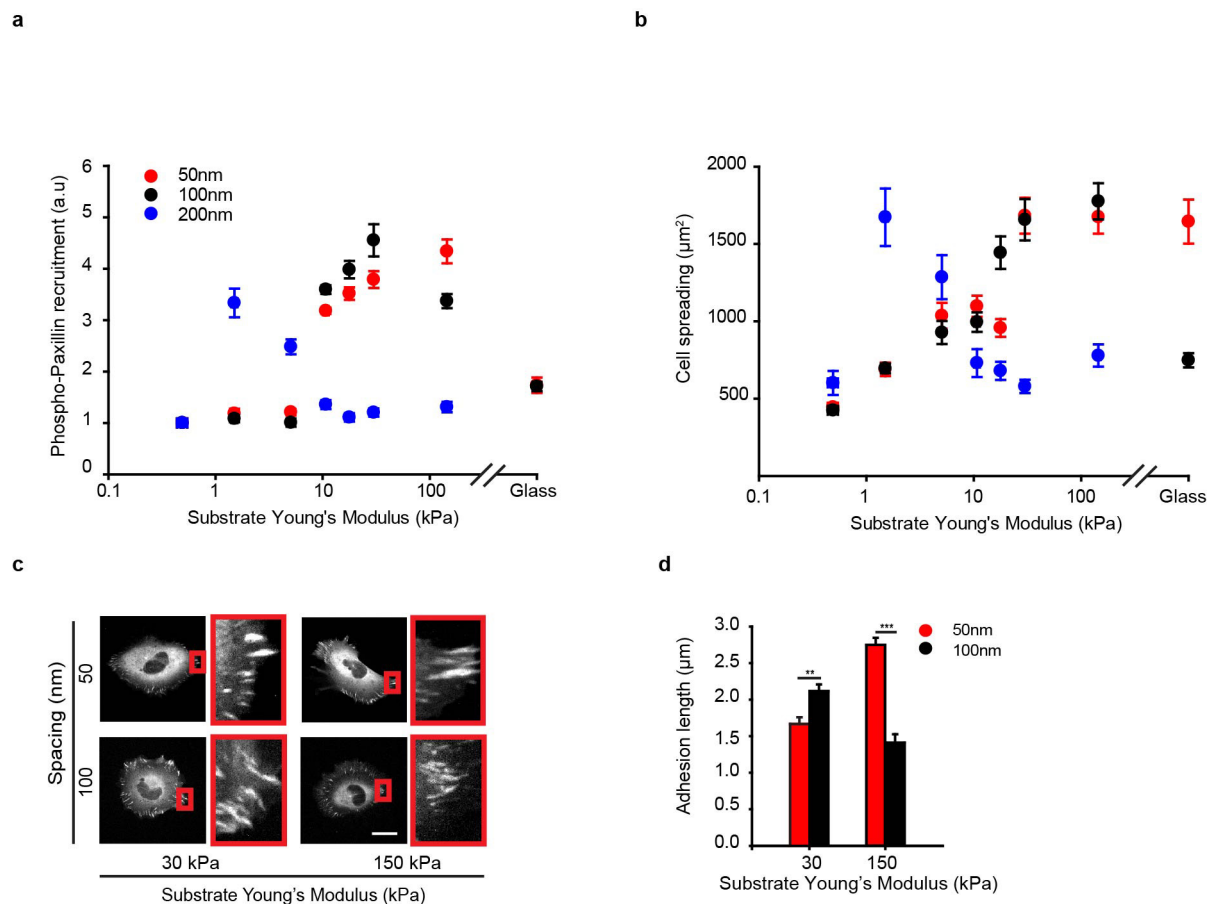**Extended Data Figure 1 | Nanopattern swelling on gels. a**, Scanning electron micrograph of a quasi-hexagonal 100-nm ordered pattern on a glass surface (from one of two independent experiments). **b**, Scanning electron micrograph of a quasi-hexagonal 100-nm ordered pattern on a polyacrylamide gel. **c**, Corresponding histograms showing the distribution of distances between nanodots and their first-order neighbours on glass and polyacrylamide substrates of rigidity 30 kPa (300 particles; two independent experiments). **d**, Corresponding quantification of mean distance between nanodots on polyacrylamide gels as a function of rigidity ($n = 300$ particles per condition; two independent experiments). Scale bar, 200 nm.
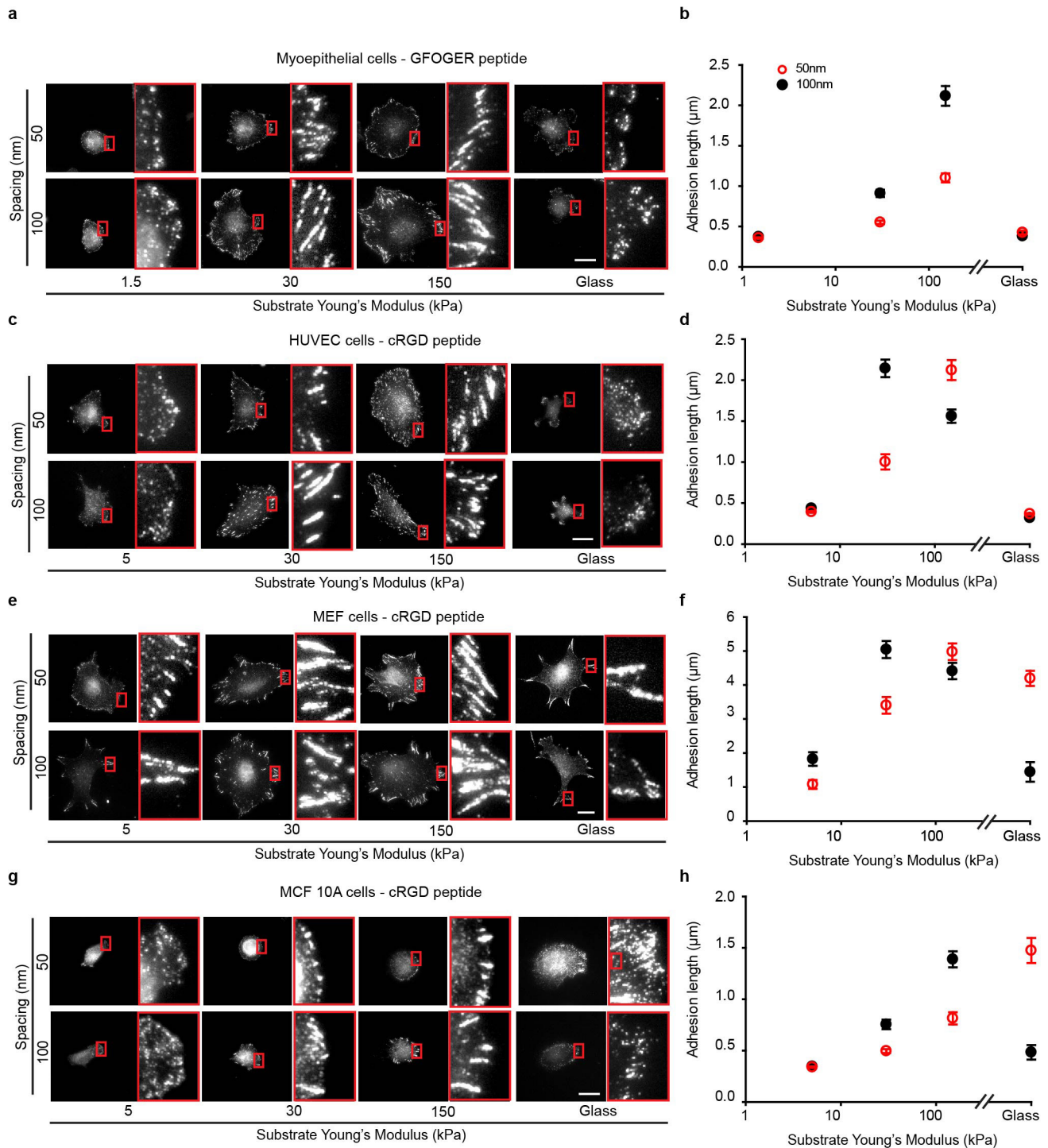
a

b

Extended Data Figure 2 | Cell binding to nanopatterned substrates is specific to α5β1 integrins, cRGD, and nanodots. a, Images showing breast myoepithelial cells plated on 30 kPa substrates with ligand spacing of 50 nm, under conditions that either allow integrin-mediated cell binding (cRGD + nanodots; top left) or do not (the remaining three images). RGE is a peptide with low affinity for α5β1 integrin; abα5β1 is an antibody that blocks α5β1 integrin. **b**, Corresponding quantification of the percentage spread of cells ($n = 30/30/30/22$ fields of view; three independent experiments). Scale bar, 100 μm; ***, $P < 0.001$. Error bars, mean ± s.e.m.
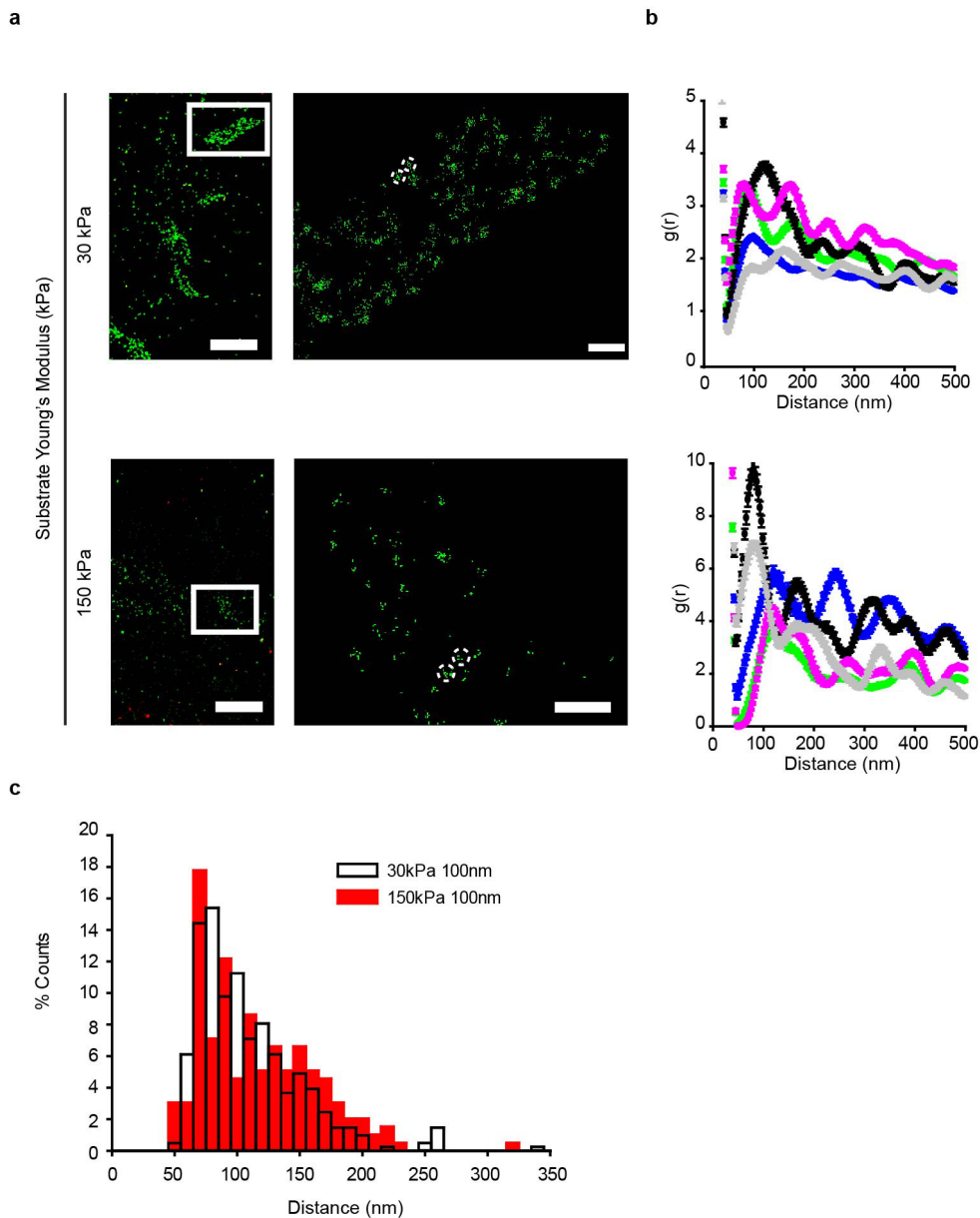
a

b

c

d

Extended Data Figure 3 | Further characterization of cell response to rigidity and nanodot spacing. a, Quantification of the fluorescence intensity of staining for phosphorylated paxillin (phospho-paxillin) at the cell edge (two different regions per cell; $n = 10/10/11$, $10/10/11$, $10/11/11$, $10/10/11$, $10/10/11$, $10/10/11$, $10/10/11$, $10/10/11$ cells on 50/100/200-nm-spaced substrates and increasing rigidity; two independent experiments). The effect of both ligand spacing and rigidity was significant ($P < 0.05$; two-way ANOVA). Rather than measuring focal adhesions, this complementary measurement integrates phospho-paxillin recruitment in both adhesions and surrounding areas. The same trends were observed in Fig. 1e. **b**, Cell-spreading area ($n = 13/13/11$, $11/16/11$, $11/19/11$, $16/13/11$, $13/16/11$, $13/14/11$, $13/13/11$ cells on 50/100/200-nm-spaced substrates

as rigidity increases; two independent experiments). Although nanodot spacing did affect cell spreading, we note that, on the 50-nm- and 100-nm-spaced substrates, the rigidities inducing adhesion formation and collapse are not associated with changes in cell spreading. **c**, Examples of cells transfected with GFP−paxillin, seeded on 30 kPa and 150 kPa substrates, with nanodots spaced 50 nm and 100 nm apart. The right-hand images of each pair correspond to rectangles marked in red in the left-hand image. **d**, Corresponding quantification of focal-adhesion length (ten adhesions per cell; $n = 11/11$, $10/10$ cells for 50/100-nm-spaced substrates as rigidity increases; two independent experiments) **, $P < 0.005$; ***, $P < 0.001$, two-way ANOVA. Scale bar, 20 μm. Error bars, mean ± s.e.m.
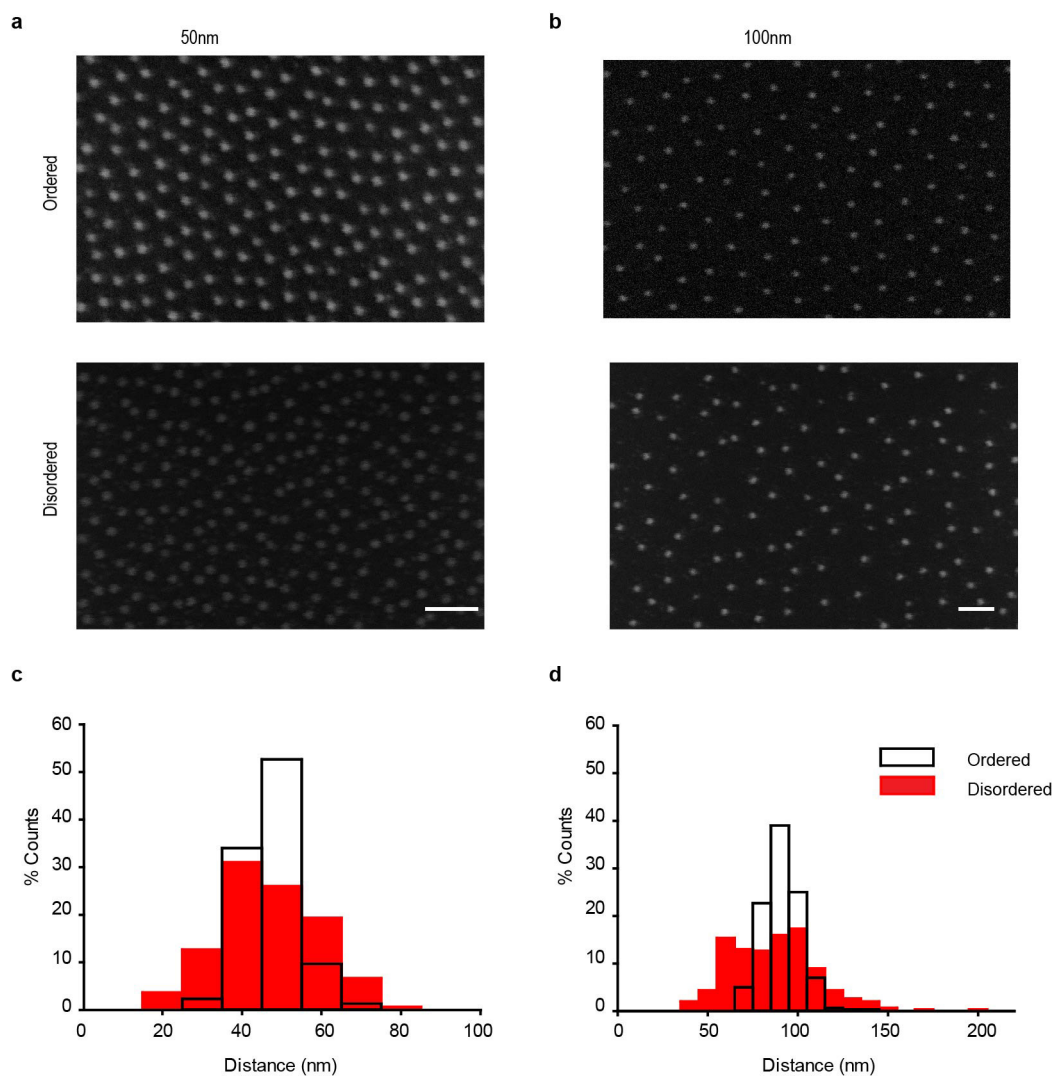
Extended Data Figure 4 | Effect of rigidity and nanodot spacing on different cell types and ligands. a, Staining of phospho-paxillin-containing adhesions in myoepithelial cells, seeded on polyacrylamide substrates of different rigidities or on glass, with either 50-nm- or 100-nm-spaced nanodots coated with the collagen-mimicking GFOGER peptide. Right-hand images are magnifications of the red rectangular regions in the left-hand images. **b**, Corresponding quantification of focal-adhesion length (mean of at least three adhesions per cell for $n = 15$ cells per condition; two independent experiments). **c–h**, As for panels **a** and **b**, but for different cell types (HUVECs, MEFs or MCF 10As) seeded on cRGD-coated nanodots. At least three focal adhesions were analysed per cell. For 50/100-nm-spaced substrates and increasing rigidity, $n = 16/16$, $16/15$, $15/16$, $15/15$ cells (HUVECs), $n = 15/15$, $16/15$, $15/15$, $14/14$ cells (MEFs), and $n = 15/15$, $15/15$, $15/15$, $10/10$ cells (MCF 10As); two independent experiments. Scale bars, 20 μm. Error bars, mean ± s.e.m.

a

Substrate Young's Modulus (kPa)

30 kPa

150 kPa

b

c

Extended Data Figure 5 | Adhesion collapse is not associated with changes in nanodot spacing between paxillin clusters. a, STORM super-resolution images of phospho-paxillin stainings in cells seeded on 100-nm-spaced patterns on 30 kPa or 150 kPa gels. Left, overview images of different focal adhesions; scale bar, 5 μm. Right, magnified images; scale bar, 300 nm. White circles show examples of phospho-paxillin clusters. Two independent experiments. **b**, Pair-correlation functions (g(r)) of phospho-paxillin clusters as a function of distance in different adhesions (marked with different colours). In all cases, a first peak is observed at around 100 nm, indicating the periodicity of the cluster pattern. **c**, Histogram showing the distances between neighbouring phospho-paxillin clusters ($n = 409$ and 197 clusters for 30 kPa and 150 kPa substrates respectively; two independent experiments). No significant differences were observed.

Extended Data Figure 6 | Spatial distribution of ordered and disordered nanopatterns. a, **b**, Scanning electron micrographs of ordered and disordered nanopatterns on glass for average nanodot spacings of 50 nm (**a**) and 100 nm (**b**). Two independent experiments. **c**, **d**, Histograms showing the distribution of interparticle distances for ordered and disordered patterns with spacings of 50 nm (**c**) and 100 nm (**d**) ($n = 300$ particles for all the conditions measured in two independent experiments). Scale bar, 100 nm.

Extended Data Table 1 | Model parameters

Parameter	meaning	Value	Origin
n_m	Number of myosin motors	190	Adjusted
F_m	Myosin motor stall force	2 pN	Ref. 43
v_u	Unloaded myosin motor velocity	90 nm/s	Values measured here and Ref. 24
n_l	Number of ligands (cRGD-functionalized nano-dots)	180 (50 nm) 130 (100 nm) 5 (200 nm)	Adjusted
d_{int}	Initial integrin density on the membrane	300/μm^2	Ref. 10
d_{intmax}	Maximum integrin density on the membrane	2200/μm^2	Adjusted
k_{ont}	True binding rate	2.31x10^{-4} um^2/s	Adjusted, of the order of values reported for αIIbβ3 Ref.44
k_{off}	Unbinding rate, scaling factor applied to force curve reported in [45]	0.5	Adjusted, catch bond dependency from Ref. 41
$F_{threshold}$	Threshold reinforcement force	87 pN	Adjusted, of the order of reported values Ref. 45
d_{add}	Integrins added after each reinforcement event	120/μm^2	Does not affect model output
a	Radius of adhesion	750 nm	Adjusted
k_{link}/k_{sub}	Elastic coupling between ligands	10 (50 nm) 5 (100 nm) 3 (200 nm)	Adjusted

Where indicated, data are from refs 10, 24, 41, 43–45.

Extended Data Table 2 | Preparation details on micellar nanolithography

Generated structures	Styrene units (x)	Vinyl-pyridine units (y)	c in mg/ml	Loading parameter of HAuCl₄	Spin coating speed in rpm
200 nm ordered	5348	713	2	0.5	11000
100 nm ordered	1824	523	4	0.6	10000
100 nm disordered	* 1824 † 123000	523	4 8	0.5	8000
50 nm ordered	1056	495	8	0.5	7000
50 nm disordered	* 1056 † 50 000	671	9 8	0.3	5000

In disordered structures, * and † refer to micellar and polystyrene solutions, respectively.

Extended Data Table 3 | Polyacrylamide gel rigidities measured by atomic force microscopy

% Acrylamide	% Bis-Acrylamide	Young's Modulus (kPa) Mean ±s.e.m.)	Number of gels
4	0.03	0.49±0.05	6
5	0.04	1.50±0.09	6
7.46	0.044	5.06±0.13	6
7.5	0.1	10.72±0.71	6
7.55	0.16	17.76±0.67	6
12	0.15	30.02±0.56	6
12	0.6	144.88±6.6	6

natureresearch

Corresponding author(s): Pere Roca-Cusachs

☐ Initial submission ☐ Revised version ☒ Final submission

Life Sciences Reporting Summary

Nature Research wishes to improve the reproducibility of the work that we publish. This form is intended for publication with all accepted life science papers and provides structure for consistency and transparency in reporting. Every life science submission will use this form; some list items might not apply to an individual manuscript, but all fields must be completed for clarity.

For further information on the points included in this form, see Reporting Life Sciences Research. For further information on Nature Research policies, including our data availability policy, see Authors & Referees and the Editorial Policy Checklist.

▶ Experimental design

1. Sample size

Describe how sample size was determined.

No statistical methods were used to predetermine sample size. During experiments, we determined that a sample size of about 10-15 was sufficient to assess whether the order of differences between conditions expected from our compuctional model were found.

2. Data exclusions

Describe any data exclusions.

No data were excluded from the analyses.

3. Replication

Describe whether the experimental findings were reliably reproduced.

All experimental findings were reproduced independently at least two times.

4. Randomization

Describe how samples/organisms/participants were allocated into experimental groups.

Cells were measured at random within each condition.

5. Blinding

Describe whether the investigators were blinded to group allocation during data collection and/or analysis.

N/A

Note: all studies involving animals and/or human research participants must disclose whether blinding and randomization were used.

6. Statistical parameters

For all figures and tables that use statistical methods, confirm that the following items are present in relevant figure legends (or in the Methods section if additional space is needed).

n/a	Confirmed	
☐	☒	The exact sample size (n) for each experimental group/condition, given as a discrete number and unit of measurement (animals, litters, cultures, etc.)
☐	☒	A description of how samples were collected, noting whether measurements were taken from distinct samples or whether the same sample was measured repeatedly
☐	☒	A statement indicating how many times each experiment was replicated
☐	☒	The statistical test(s) used and whether they are one- or two-sided (note: only common tests should be described solely by name; more complex techniques should be described in the Methods section)
☐	☒	A description of any assumptions or corrections, such as an adjustment for multiple comparisons
☐	☒	The test results (e.g. P values) given as exact values whenever possible and with confidence intervals noted
☐	☒	A clear description of statistics including central tendency (e.g. median, mean) and variation (e.g. standard deviation, interquartile range)
☐	☒	Clearly defined error bars

See the web collection on statistics for biologists for further resources and guidance.

▶ Software

7. Software

Describe the software used to analyze the data in this study.

Custom code in Matlab was employed to implement the computational clutch model, and to calculate traction forces.

For manuscripts utilizing custom algorithms or software that are central to the paper but not yet described in the published literature, software must be made available to editors and reviewers upon request. We strongly encourage code deposition in a community repository (e.g. GitHub). *Nature Methods* guidance for providing algorithms and software for publication provides further information on this topic.

▶ Materials and reagents

8. Materials availability

Indicate whether there are restrictions on availability of unique materials or if these materials are only available for distribution by a for-profit company.

No unique materials were used.

9. Antibodies

Describe the antibodies used and how they were validated for use in the system under study (i.e. assay and species).

α5β1 blocking integrin blocking antibody (30ug/ml, clone JBS5 - MAB1969, Millipore)
Phospho-paxillin antibody(Cell Signaling 2541S, 1:50 dilution)
YAP antibody (clone 63.7 produced in mouse, Santa Cruz catalogue no. sc-101199, 1:200 dilution)
All antibodies are validated for the species and assay used as described in the manufacturer's web page.

10. Eukaryotic cell lines

a. State the source of each eukaryotic cell line used.

Human breast myoepithelial immortalized cell lines were described previously (supplementary refs 4,5 of the paper). Human umbilical vein endothelial cells were purchased from Lonza (CC-2517). Mouse Embryonic fibroblasts were described previously (supplementary ref. 6 of the paper). Mammary epithelial cells (MCF10A) were purchased from ATCC.

b. Describe the method of cell line authentication used.

Myoepithelial cells used throughout the manuscript were authenticated in their lab of origin through expression of Integrin β4 , P-cadherin, cytokeratin 17, and desmoglein 3. Other cell lines (used only to verify the generality of our findings) were not authenticated.

c. Report whether the cell lines were tested for mycoplasma contamination.

All cell lines tested negative for mycoplasma contamination.

d. If any of the cell lines used are listed in the database of commonly misidentified cell lines maintained by ICLAC, provide a scientific rationale for their use.

No commonly misidentified cell lines were used.

▶ Animals and human research participants

11. Description of research animals

Provide details on animals and/or animal-derived materials used in the study.

No animals were used.

12. Description of human research participants

Describe the covariate-relevant population characteristics of the human research participants.

This study did not involve human research participants.